processes

MDPI

Article

Adsorption of Low Density Lipoproteins on an Azobenzene-Containing Polymer Brush: Modelling by Coarse-Grained Molecular Dynamics

Jaroslav Ilnytskyi [1,2,*], Dmytro Yaremchuk [1] and Orest Komarytsia [3]

[1] Department of Computer Simulations of the Many-Particle Systems, Institute for Condensed Matter Physics of the National Academy of Sciences of Ukraine, 79011 Lviv, Ukraine; yaremchuk@icmp.lviv.ua
[2] Department of Applied Mathematics, Institute of Applied Mathematics and Fundamental Sciences, Lviv Polytechnic National University, 79013 Lviv, Ukraine
[3] Department of Internal Medicine 2, Danylo Halytskyi Lviv Medical lUniversity, 79010 Lviv, Ukraine; kaf_internalmed_2@meduniv.lviv.ua
* Correspondence: iln@icmp.lviv.ua

Abstract: One of the strategies to reduce the contents of low density lipoproteins (LDLs) in blood is a hemoperfusion, when they are selectively retracted from plasma by an adsorber located outside the patient's body. Recently, a photo-controllable smart surface was developed experimentally, that is characterized by high selectivity and reusability. It comprises a nanocarrier functionalised by a brush of azobenzene-containing polymer chains. We present a mesoscopic model that mimics principal features of this setup and focus our study on the role played by the length and flexibility of the chains and grafting density of a brush. The model for LDL comprises a spherical core covered by a shell of model phospholipids. The model is studied via coarse-grained molecular dynamics simulation, performed with the aid of the GMBOLDD package modified for the case of soft-core beads. We examined the dependencies of the binding energy on both the length of polymer chains and the grafting density of a brush and established optimal conditions for adsorption. These are explained by competition between the concentration of azobenzenes and phospholipids in the same spatial region, flexibility of polymer chains, and excluded volume effects.

Keywords: low density lipoproteins; hemoperfusion; azobenzene; adsorption; molecular dynamics

Citation: Ilnytskyi, J.; Yaremchuk, D.; Komarytsia, O. Adsorption of Low Density Lipoproteins on an Azobenzene-Containing Polymer Brush: Modelling by Coarse-Grained Molecular Dynamics. *Processes* **2023**, *11*, 2913. https://doi.org/10.3390/pr11102913

Academic Editor: Olga Guskova

Received: 1 September 2023
Revised: 28 September 2023
Accepted: 29 September 2023
Published: 4 October 2023

1. Introduction

Lipoproteins are the major carriers of cholesterol within a human body and, therefore, are of great importance for metabolic processes. Low-density lipoproteins (LDL) bring cholesterol from liver to cells, whereas high-density lipoproteins (HDL) carry cholesterol from the heart and other organs back to the liver, where it is removed out of the body. LDL may cause cholesterol to build up within arteries and can eventually block arteries, increasing the risk for heart disease and stroke [1–5]. The indication of the increased risk of this scenario is an abnormally high level of LDL.

Two main strategies exist to reduce the risk of such a blockade: (i) by treating the blood vessels (stenting or stents implantation) or (ii) by reducing the high concentration of LDL in blood. The latter can be seen rather as the preventive approach with two ways of realization: (a) in-body reduction by affecting liver activity (using statins) or digesting adsorbers and (b) the hemoperfusion approach, when adsorbers are located outside the body [6].

In dealing with atherosclerosis, which is characterized by an increased level of the total LDL cholesterol, pharmacological groups of drugs are widely and primarily used, with statins occupying the first place. The second- and third-line drugs used for this purpose are ezetimibe and fibrates. Currently, drugs combining statins and ezetimibe demonstrate

particular effectiveness in this respect. Intolerance of hypolipidemic drugs manifests itself via (a) unwanted symptoms perceived by patients as unacceptable and/or (b) abnormal laboratory results that indicate an excessive risk associated with the use of hypolipidemic drugs. In both cases, such drugs are withdrawn. Such patients, characterized by either absolute or relative intolerance to this type of treatment, are the first candidates for full or partial hemoperfusion therapy.

In a course of adsorbent-based hemoperfusion, the patient's blood is introduced into a container with the specific adsorbent. It binds LDL selectively and, at the same time, allows the HDL and other blood components to pass through and then be re-introduced into the patient's body. Several types of hemoperfusion adsorbents are used in clinical practice, including biomacromolecules, magnetic nanoparticles, carbon nanotubes, nanohydrogels, and porous beads [1,2,6]. The main goal is to achieve efficiency and high selectivity of LDL removal and reusability of the adsorbent.

Amphiphilic polymers were used by Cheng et al. [7], which, at a particular sulfonation rate and cholesterol grafting time, demonstrated highly selective LDL adsorption. After 2 h hemoperfusion, LDL levels decreased by a fraction of five. To achieve the binding of LDL with high affinity, the biomimetic adsorbent was developed by Yu et al. [6], which mimics the lipoprotein microemulsion present in the blood. In vitro studies revealed the LDL adsorption rate was about twice as high as that of the HDL. In yet another work, the core-shell structured magnetic nanoparticles were embedded in an amphiphilic polymer layer to provide multifunctional, highly selective binding for LDL particles [8]. Due to the electronegativity of the functional layer and charged surface of LDL, the nano-adsorbent demonstrated highly selective adsorption towards LDL, whereas chemical adsorption also plays a predominant role in binding of LDL. This nano-adsorbent possesses satisfactory recyclability, low cytotoxicity, and hemolysis ratios [8].

Controllability of the adsorption can be achieved by means of "smart surfaces", i.e., the thermo- [9–11], magnetically- [12], and photo- [13] controllable surfaces [14]. Thermo-controllable surfaces, based on a PNIPAM polymer, have already found numerous biomedical applications [9]. The photo-controllability of the surface properties is achieved by incorporating some photosensitive group into it, with the azobenzene chromophore being the most widely used one [15]. Such "azobenzination" allows a number of features of the smart surface, namely: the control over adhesive properties of a surface [16], manipulation of nano objects on it [17], photo-controllable separation of a photoresponsive surfactant from the adsorbate [18], achieving photo-reversible surface polarity [19], photo-controllable orientational order affecting surface anchoring of liquid crytals [20], etc. Recently, the advanced LDL adsorber in the form of a photo-controllable smart surface was developed, characterised by high selectivity and reusability [21]. It exhibited excellent LDL adsorption capacity and could be regenerated by illumination with high efficiency, further verified by transmission electron microscopy and Fourier-transform infrared analysis. Green regeneration of the nano-adsorbent could be achieved completely through a simple photoregeneration process, and the recovery rate was still 97.9% after five regeneration experiments [21].

This experimental work sparked our interest towards modelling the process of LDL adsorption by such an advanced photo-controllable adsorber by employing computer simulations. One should note that the native length scale of the problem, complexity, and ambiguity of the LDL structure [2,22–29] prevent performing atomistic-scale simulation of such a process in the foreseen future. There are a number of computer simulation studies performed mostly on a coarse-grained level that address the structure of LDL, lipid transport, receptor mutations, and other related topics [30–39].

We see the possibility of performing the coarse-grained simulations of the adsorption of LDL particles explicitly if one uses:

1. A minimalistic model containing only the elements directly involved in adsorption;
2. Reduction of the length scale of a problem;
3. Artificial speed-up of system dynamics.

In doing this, we follow our previous studies on modelling photo-sensitive polymers using coarse-grained simulations [40–44]. The modelling approach is covered in detail in Section 2. Ideally, such simulations would provide important insights on the polymer architecture of the photo-controllable adsorber that are needed to improve its efficiency. These might be further used for refining synthesis protocols. On a minimalistic side, such simulations would validate the suggested type of modelling by comparing their results against observed experimental features.

The outline of this study is as follows. In the first part of Section 2, we review available experimental data on the overall shape and internal structure of LDL and on its photo-controllable adsorption. It sets the basis for constructing the coarse-grained model for the problem of interest, covered in detail in the second part of this section. Section 3 contains the results of the computer simulation of this model mimicking the adsorption of LDL under visible light, whereas Section 4 focuses on the adsorber regeneration under ultraviolet light, followed by conclusions.

2. Experimental Data on LDL Structure and the Modelling Details

In general, plasma LDLs are heterogeneous in **size**, as well as their density and lipid content. Two following types of LDL were identified: larger, pattern A type of an average dimension larger than 25.5 nm; and pattern B of a smaller average dimension less than 25.5 nm [45]. The latter ones are found to be more prevalent in patients with coronary artery disease [46], with a higher risk of myocardial infarction [47] and of developing coronary disease [48,49]. The reason for this could be their reduced affinity for the respective receptor and, as a result, an increased residence time in plasma and higher probability to be oxidised at the artery walls, leading to atherosclerosis [50]. Therefore, the pattern B LDL of an estimated diameter of 20 to 23 nm [50] is the main target for adsorption via hemoperfusion.

In terms of their **internal structure**, the LDL particles can be interpreted as micellar complexes, macromolecular assemblies, self-organised nanoparticles, or microemulsions [26,29]. A spherical three-layer model has been suggested based on the low-resolution data [24,25]. It assumes the presence of an internal core of LDL comprising cholesteryl ester and triglycerides. The core is enveloped by an outer shell of phospholipids, with their polar heads residing on the surface of LDL and their fatty acid ester tails pointing inward to the LDL. About half of the external surface of LDL is covered with apolipoprotein B-100, which form ligand recognition loops for various receptors [2,23]. In particular, the B-100 in a form of two ring-shaped structures were reported [22]. A liquid crystalline core model of LDL was also discussed [27].

Complexity of the internal structure affects the overall LDL **shape** and the spherical [25], discotic [22,26], as well full range of spherical, discotic, and ellipsoidal [27] shapes all were reported. A possible explanation for these discrepancies is the effect of the temperature on the arrangement of cholesteryl ester molecules in the LDL core. As a result, at physiological temperatures, LDL appears more spherical, whereas at lower temperatures, discoidal [28]. Indeed, the discotic shape was predominantly found by means of cryo-electron microscopy [22,23,26,27] performed at low temperatures.

These experimental findings lay out the basis for developing a range of moderately coarse-grained **models** of LDL. These type of lipid simulations [31] can address two main issues. The first one is to improve one's understanding of the internal LDL structure [30,32], addressing mutational space of the LDL receptor [37], etc. The other is to understand the physical chemistry mechanisms behind the lipid transfer [33,36,38,39]. On a more coarse-grained level, the interactions between oxidised LDL and scavenger receptors on the cell surfaces of macrophages, related to arterial stiffening, are addressed [34]. The smectic-isotropic transition inside the LDL core, related to the liquid crystalline order found there in Ref. [27], was modelled in Ref. [35].

The **modelling approach** developed in this study follows the coarse-graining plan outlined in Section 1. According to statement (1) there, the model contains only the elements directly involved in adsorption setup by Guo et al. [21]. In their setup, the

nanoadsorbers consist of a spherical support particle of a diameter of 200 nm functionalised by the azobenzene-containing polymers. The ratio between the diameters of a nanoadsorber and that of LDL is about 10:1. This results in relatively low curvature of a nanoadsorber comparing to the LDL size, and, therefore, one can approximate a surface of a former by a flat surface. This is conducted in our study. The model contains two adsorbing surfaces on both the bottom, $z = 0$, and the top, $z = L_z$, walls of the simulation box with dimensions L_x, L_y, and L_z. By using two walls instead of a single one, one (i) avoids possible artefacts at the top free wall and (ii) improves the statistics obtained in the course of a single simulation run. The polymers are of the side-chain architecture [6], with their side chains terminated by azobenzenes [21]; their representation via a set of coarse-graining beads is shown in Figure 1.

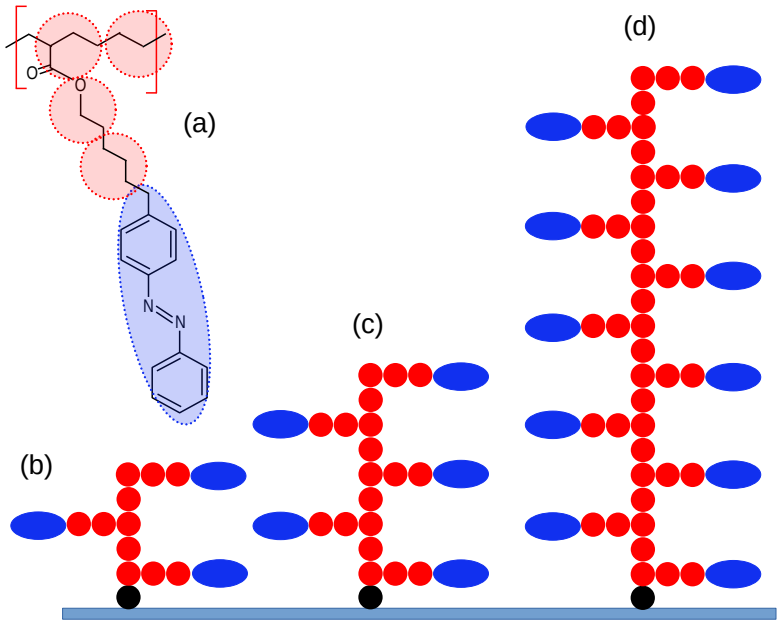

Figure 1. (**a**) A scheme showing coarse-graining of the azobenzene-containing polyacrylate. Spherical beads (shown as transparent red spheres) represent approximately three heavy atoms. The azobenzene groups are modelled by rigid elongated objects, shown in a transparent blue colour. (**b**) Model azobenzene-containing polymer chain of the backbone length of $l_{bb} = 6$. Red and blue beads represent atomic groups according to Figure (**a**); the first bead displayed in black is grafted to the substrate, which is shown as a gray-blue bar at the bottom of the figure. (**c**,**d**) show the same chains as in Figure (**b**) but of a larger backbone length of $l_{bb} = 10$ and 22.

Similarly, only the structure elements of the LDLs that are relevant to their adsorption are modelled explicitly. We consider physiological temperature, where the LDL core is of a spherical shape [28]. It is filled by cholesteryl esters and triglycerides (see Figure 2a). This part of LDL is not involved in adsorption in a direct way and is replaced in our model by a uniform spherical object, as shown in (b). The outer shell of LDL is involved in adsorption explicitly, via the interaction of phospholipids with the azobenzenes of a brush. This shell is modelled as a collection of elongated particles representing coarse-graining of phospholipids (see Figure 2b,c).

Similar coarse-grained building blocks, alongside the force-field parameters, were used and tested in a set of our previous works involving polymer brushes and decorated nanoparticles [40,41,43,51,52]. The length scale of a model is set by the coarse-graining procedure for a brush, as shown in Figure 1, and it follows approximately the real physical units. Simulation of a set of LDL particles in this scale is prohibitively expensive. Therefore, we reduced the diameter of the LDL particles to 5 nm, about five times comparing to a real

size of these objects. The effect of reduced size for the LDL particles is discussed in the results section.

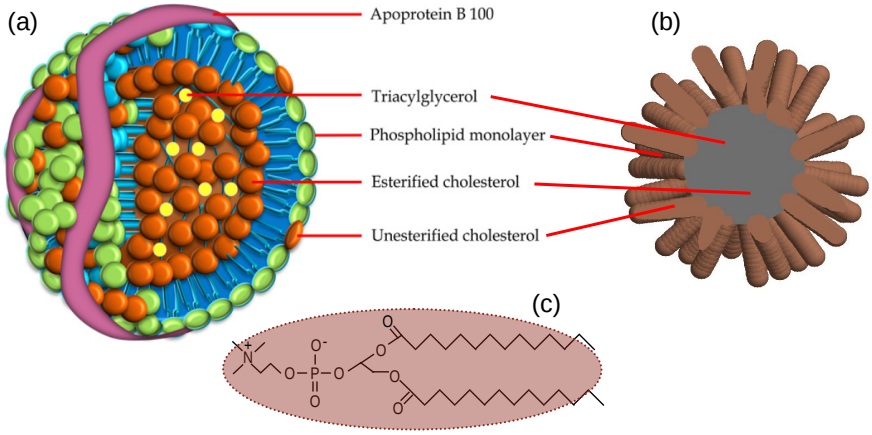

Figure 2. (**a**) Internal structure of the LDL particle, reprinted from [53] under Creative Commons 4.0 International License. (**b**) Model LDL particle: grey sphere represents central uniform core, brown spherocylinders mimic model phospholipid units. (**c**) Coarse-graining of phospholipid molecule unit.

We provide the dimensions of the model building blocks here. The monomers of backbones and of side chains are represented by soft-core spherical beads of a diameter of $\sigma = 0.46\,\mathrm{nm}$, mimicking approximately a group of three hydrocarbons each [54] (see Figure 1a). Each second bead of a backbone is as a branching point for a side chain of two spherical beads terminated by an azobenzene, as shown in Figure 1b–d of the same Figure 1. The latter is modelled as a soft-core spherocylinder with the diameter of a spherical cap equal to $D = 0.37\,\mathrm{nm}$ and a length-to-breadth ratio of $L/D = 3$, resulting in a total length of a spherocylinder of $D/2 + L + D/2 = 4D \approx 1.5\,\mathrm{nm}$. Phospholipids are modelled by the same type of prolate particles as the azobenzenes to simplify modelling. The packing density of phospholipids in the outer shell will affect adsorption; therefore, we provide an estimate for it here. The model comprises 100 phospholipids per each LDL, then the area packing fraction of their ends on the core surface is about $\eta = 0.77$. This value is reasonable. In particular, in the coarse-grained simulations of a single LDL by Murtola et al. [32], the diameter of the LDL was 18 nm. Its outer shell has a surface area of about $1000\,\mathrm{nm}^2$ and contained in total 1300 phospholipids and unesterified cholesterols. Assuming that one molecule occupies roughly a square region of $0.78\,\mathrm{nm}^2$ [55], this corresponds to a disc with an area of $0.6\,\mathrm{nm}^2$. Then, we arrive at the surface packing fraction of about $\eta' = 0.78$, whis is very close to η estimated above. These packing densities are close to the maximum packing fraction of discs arranged on a $2D$ square lattice, $\eta'' = \pi/4 \approx 0.79$.

Here, we use the coarse-grained interaction potentials obtained from atomistic modelling [54]; however, their forms are rather generic and reflect the shape and the main features of interacting beads [56]. Therefore, these potentials are not specifically tuned to mimic a certain compound but are aimed at a description of universal physical features of a wider class of polymers. By using soft-core spherical and spherocylinder beads, one greatly speeds up the dynamics in a system, hence, implementing statement (3) of the coarse-graining plan enlisted in Section 1.

To simplify expressions for the non-bonded interactions, each pair $\{i, j\}$ of the particles is characterised by a shorthand containing a set of variables, $\mathbf{q}_{ij} = \{\widehat{\mathbf{e}}_i, \widehat{\mathbf{e}}_j, \mathbf{r}_{ij}\}$, where $\widehat{\mathbf{e}}_i$ and $\widehat{\mathbf{e}}_j$ are the unit vectors defining the orientation of the respective particles in space, and $\mathbf{r}_{ij}$ is the vector that connects their centers of mass. For the case of spherical particles, their orientations are not defined. The Kihara type of potential, used here, implies evaluation of the closest distance, $d(\mathbf{q}_{ij})$, between the internal cores of two interacting particles, where the core of a spherical particle is its center, and the core of a spherocylinder is the line connecting the centers of its two spherical caps. The scaling factor σ_{ij} is evaluated for the

pair, where $\sigma_{ij} = (\sigma_i + \sigma_j)/2$ for two spherical particles, $\sigma_{ij} = D$ for two spherocylinder particles, and $\sigma_{ij} = (\sigma_i + D)/2$ for the mixed sphere-spherocylinder pair. The dimensionless closest distance between two interacting particles is defined then as $d'(\mathbf{q}_{ij}) = d(\mathbf{q}_{ij})/\sigma_{ij}$.

Using these notations, the general form of the pair interaction potential between ith and jth beads, that is, of the soft attractive (SAP) type [56], can be written in a compact dimensionless form

$$V_{\mathrm{NB}}^{\mathrm{SAP}}[d'(\mathbf{q}_{ij})] = \begin{cases} U\{[1-d'(\mathbf{q}_{ij})]^2 - \epsilon'(\mathbf{q}_{ij})\}, & 0 \le d'(\mathbf{q}_{ij}) < 1 \\ U\{[1-d'(\mathbf{q}_{ij})]^2 - \epsilon'(\mathbf{q}_{ij}) & \\ \quad - \frac{1}{4\epsilon'(\mathbf{q}_{ij})}[1-d'(\mathbf{q}_{ij})]^4\}, & 1 \le d'(\mathbf{q}_{ij}) \le d'_c \\ 0, & d'(\mathbf{q}_{ij}) > d'_c \end{cases} \tag{1}$$

where U defines repulsion strength. The dimensionless well depth of this potential

$$\epsilon'(\mathbf{q}_{ij}) = \left\{ 4\left[U'_a - 5\epsilon'_1 P_2(\widehat{\mathbf{e}}_i \cdot \widehat{\mathbf{e}}_j) - 5\epsilon'_2 \left(P_2(\widehat{\mathbf{r}}_{ij} \cdot \widehat{\mathbf{e}}_i) + P_2(\widehat{\mathbf{r}}_{ij} \cdot \widehat{\mathbf{e}}_j) \right) \right] \right\}^{-1}, \tag{2}$$

is obtained from the condition that both the expression (1) and its first derivative on $d'(\mathbf{q}_{ij})$ turn to zero when $d'(\mathbf{q}_{ij}) = d'_c$, where $d'_c = 1 + \sqrt{2\epsilon'(\mathbf{q}_{ij})}$ is the cutoff separation for the potential [56]. Here, $\widehat{\mathbf{r}}_{ij} = \mathbf{r}_{ij}/r_{ij}$ is a unit vector along the line connecting the centers of two beads, and U'_a, ϵ'_1, and ϵ'_2 are dimensionless parameters that define the shape of the interaction potential. These are chosen to represent the "model A" of Ref. [56]. $P_2(x) = (3x^2 - 1)/2$ is the second Legendre polynomial.

The effective well depth, $\epsilon'(\mathbf{q}_{ij})$, influences both the shape of the attractive part and, via d'_c, its range. When the parameters, contained in the expression for $\epsilon'(\mathbf{q}_{ij})$, are such that it asymptotically reaches zero, the cutoff d'_c approaches 1 and the interval for the second line in Equation (1) shrinks to zero. As a result, in this limit, one retrieves the soft repulsive potential (SRP) of a quadratic form

$$V_{\mathrm{NB}}^{\mathrm{SRP}}[d'(\mathbf{q}_{ij})] = \begin{cases} U\left[1-d'(\mathbf{q}_{ij})\right]^2, & 0 \le d'(\mathbf{q}_{ij}) \le 1 \\ 0, & d'(\mathbf{q}_{ij}) > 1 \end{cases} \tag{3}$$

that is used typically in the dissipative particle dynamics simulations [57]. This limit is illustrated in Figure 3 by the blue curve and is marked as $\epsilon'(\mathbf{q}_{ij}) \to 0$.

Attractive potential (1) is used to model the interaction between the *trans*-azobenzene and a phospholipid only. The origin of their attraction in a water-like solvent lies in strong hydrophobicity of both groups [58]. For all other pair interactions, soft repulsive potential (3) is used, reflecting the nature of the coarse-grained type of modelling. In this way, we emphasise the role of the azobenzene–phospholipid interactions as the key factor in the adsorption process. Another approach can also be employed, where the pairs of two *trans*-azobenzenes and of two phospholipids are interacting via potential (1) as well. In this case, adsorption of LDL particles will compete against both the aggregation of LDL particles and the self-collapse of the brush. We might consider this case in the future. Strong repulsion, with the energy parameter $U' = 2U$ in Equation (3), is introduced for the interaction of both *trans*-azobenzene and polymer beads with solvent, reflecting their poor solubility in water. Such type of modelling of azobenzenes has been already used in a number of previous studies [40–44].

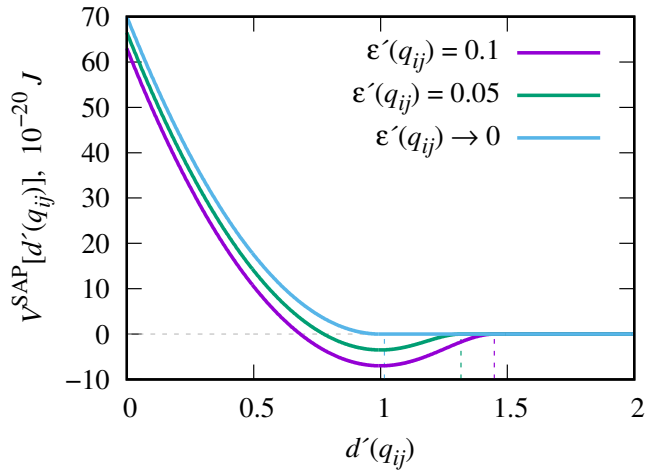

Figure 3. Illustration of the interaction potential $V^{\mathrm{SAP}}[d'(\mathbf{q}_{ij})]$ between two beads of any type shown for a range of effective dimensionless well depths $\epsilon'(\mathbf{q}_{ij})$ (respective cutoffs d'_c are indicated via vertical dashed lines). $d'(\mathbf{q}_{ij})$ is the minimum distance between the beads cores, which reduces to the dimensionless separation r'_{ij} between the centers for the case of two interacting spherical beads. At the well depth approaching zero, $\epsilon'(\mathbf{q}_{ij}) \to 0$, the potential $V^{\mathrm{SAP}}[d'(\mathbf{q}_{ij})]$ turns into a purely repulsive potential $V^{\mathrm{SRP}}[d'(\mathbf{q}_{ij})]$, Equation (3) (see blue curve in the plot).

The expressions for the total bonded interactions within the brush and within each LDL, respectively, are given as

$$V_{\mathrm{B}}^{\mathrm{BR}} = \sum_{k=1}^{N_{BR}} \left[\sum_{i=1}^{n'_b} k_b (l_i - l_0)^2 + \sum_{i=1}^{n'_a} k_a (\theta_i - \theta_0)^2 + \sum_{i=1}^{n'_z} k_z (\zeta_i - \zeta_0)^2 \right], \tag{4}$$

$$V_{\mathrm{B}}^{\mathrm{LDL}} = \sum_{k=1}^{N_{LDL}} \left[\sum_{i=1}^{n''_b} k_b (l_i - l_0)^2 + \sum_{i=1}^{n''_z} k_z (\zeta_i - \zeta_0)^2 \right], \tag{5}$$

where N_{BR} and N_{LDL} are the total number of polymer chains in a brush and of LDL particles, respectively; n'_b, n'_a, and n'_z are the numbers of bonds, branching angles, and terminal angles in a single polymer molecule, and n''_b and n''_z are the numbers of bonds and terminal angles in a single LDL particle. The purpose of bonds in LDL particles is to keep each phospholipid at a given separation from the center of a core to form the outer spherical shell. The energy term involving branching angles, θ_i, in Equation (4) maintains a certain level of perpendicularity of side chains to a local orientation of a backbone. Similarly, correct orientations ζ_i of both the azobenzenes and phospholipids, with respect to the bond by which these are attached to a spherical bead, are ensured in Equations (4) and (5) by the energy term involving the terminal angle ζ_i [59].

According to the model description provided above, the required numbers of beads and of various energy terms in a single polymer molecule can be derived from the chosen value for the backbone length, l_{bb}. Namely, each polymer contains $n_{sc} = \mathrm{div}(l_{bb}, 2)$ side chains (where div denotes division of two integers), in total $n_p = l_{bb} + 2n_{sc}$ spherical and $n_a = n_{sc}$ azobenzene beads. Therefore, the number of bonded interactions are given by: $n'_b = n_p + n_a - 1$, $n'_a = n_{sc}$, and $n'_z = n_a$. Each LDL particle consists of spherical core particles and $n_{pl} = 100$ phospholipids; therefore, $n''_b = n''_z = n_{pl}$. All force field parameters are collected in Table 1 for the sake of convenience.

Table 1. Force field parameters, derived in Refs. [51,54].

Parameter	Description	Value
σ_c	core diameter	2.14 nm
σ	monomer and solvent bead diameter	0.46 nm
D	azobenzene and phospholipid cap diameter	0.37 nm
L/D	azobenzene and phospholipid aspect ratio	3
U	energy factor for regular repulsion	70×10^{-20} J
U'	energy factor for strong repulsion	140×10^{-20} J
U'_a	attractive energy parameter	21.43
ϵ'_1	attractive energy parameter	1.714
ϵ'_2	attractive energy parameter	−1.714
m_c	core mass	62.44×10^{-25} kg
m	monomer and solvent bead mass	0.70×10^{-25} kg
m_a	azobenzene and phospholipid mass	3.94×10^{-25} kg
I_a	azobenzene and phospholipid moment of inertia	6.00×10^{-24} kg
$l_c p$	bond length: core–phospholipid	1.82 nm
l	bond length: monomer–monomer	0.36 nm
l_a	bond length: last spacer bead–azobenzene	0.3 nm
k_b	bond spring constant	5000×10^{-20} J/ nm^2
θ	pseudo-valent angle at branching points	$\pi/2$
k_a	pseudo-valent angle spring constant	20×10^{-20} J/rad^2
ζ	terminal angle for azobenzene and phospholipid	0
k_z	terminal angle for azobenzene and phospholipid spring constant	20×10^{-20} J/rad^2

Simulation runs parameters are as follows. The simulation box dimensions are: $L_x = L_y = L_y = 20$ nm, where both bottom, $z = 0$, and top, $z = L_z$, walls are functionalized by N_{BR} polymers each (see Figure 1). Polymers of five different backbone lengths, $l_{bb} = 5, 6, 10, 16$, and 22, are considered, as well as a range of brush grafting densities

$$\rho_g = N_{BR}\sigma^2/(L_x L_y). \quad (6)$$

Both characteristics affect the adsorption scenario of macromolecules by a brush, e.g., for the case of peptides [60]. The arrangement of grafting points follows the sites of the square lattice to minimise inhomogeneities in the arrangement of polymers. The number of LDL particles is constant in all cases and is equal to $N_{LDL} = 25$. The box interior is filled by beads of the same dimensions as the monomers of a brush; these represent a water-like solvent. The simulations are carried out with the GBMOLDD [61,62] program generalised for the case of coarse-grained soft-core potentials [51] in the NVT ensemble at the bulk density $\rho = 0.5\,\mathrm{g/cm^3}$ and the temperature $T = 480$ K. This choice is based on the previous findings [51], where the melt involving the spherocylinders interacting via potential (1) exhibited the order–disorder transition at about $T = 505 - 510$ K. Therefore, at $T = 480$ K, we expect strong azobenzene–phospholipid interactions. Simulation runs of a duration of 40 ns were undertaken at each polymer length and grafting density, with a time step of $\Delta t \sim 20$ fs. Due to a large difference between the masses of the constituent particles, we use a modified velocity rescaling thermostat. Namely, the model system is split into three subsystems: LDL cores, spherical beads forming polymer chains, and the model azobenzene groups. Each 20 MD steps, the velocities in each subsystem are rescaled to ensure required temperature associated with their translational, and, in the case of azobenzenes, rotational motion.

3. Adsorption of LDL at Normal Conditions

3.1. Density Profiles and the Probability of Azobenzene–Phospholipid Contact

At normal conditions, under visible light, azobenzene chromophores are found in the *trans* isomeric state [63] and exhibit properties similar to ordinary mesogens, such as cyanobiphenyls [64]. In a water environment, *trans*-azobenzene is attracted to phospholipids from an outer shell of LDL due to the strong hydrophobicity of both. This forms a basis for the adsorption of LDL onto azobenzene-containing ligands [21].

The process of gradual adsorption of LDL particles from the middle of the channel onto the polymer brushes is illustrated by a series of snapshots given in Figure 4. The case of a polymer backbone length of $l_{bb} = 10$ and brush grafting density of $\rho_g = 0.02$ is shown. Adsorption starts after about 1 ns, see Figure 4a, and partial adsorption is illustrated after 10 ns, see Figure 4b. After 40 ns, almost all available LDL particles are adsorbed on the walls, see Figure 4c. In general, a similar scenario is found for all the backbone lengths, $l_{bb} = 5 - 22$, of brush polymers and within a broad range of their grafting densities, $0.008 < \rho_g < 0.35$. As one can see in Figure 4c, in the adsorbed state, azobenzenes (shown in blue) penetrate deeply into the outer layer of LDL particles (shown in brown), in a manner anticipated in Ref. [21].

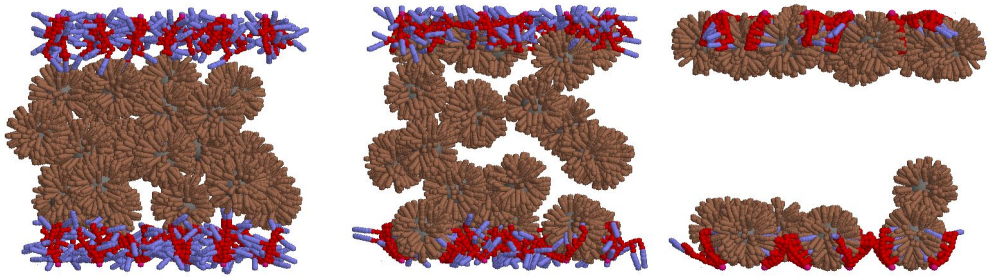

(**a**) (**b**) (**c**)

Figure 4. Snapshots showing the adsorption dynamics of LDLs on a double-wall brush composed of side-chain polymers of the backbone length $l_{bb} = 10$ (5 side chains in each chain terminated by the azobenzene bead) at a grafting density $\rho_g = 0.02$ under visible light. (**a**–**c**) visualise the system after 1 ns, 10 ns, and 40 ns, respectively. Colour coding of all beads is introduced in Figures 1 and 2. (**a**) After 1 ns; (**b**) after 10 ns; (**c**) after 40 ns.

To quantify the effects that both the backbone length, l_{bb}, and the brush grafting density, ρ_g, have on the adsorption process, we introduce a set of relevant characteristics. The obvious prerequisite for adsorption is a non-zero probability to find azobenzenes and phospholipids within the same region of space; hence, we turn our attention to the spatial distributions of these beads. According to the setup symmetry, we consider a set of slabs spanning in both OX and OY directions that are located at a certain distance z from the bottom wall. The density profiles $\rho_{az}(z)$ and $\rho_{ph}(z)$ are built for azobenzenes and phospholipids, respectively. The histograms for these profiles are shown in Figure 5 for the case of $l_{bb} = 16$ and three grafting densities ρ_g, as indicated in the figure. Note that the area under the histogram $\rho_{ph}(z)$ is constant, as $N_{LDL} = 25$ is the same in all cases. In contrast, the area under the histogram $\rho_{az}(z)$ grows upon the increase of grafting density, ρ_g, reflecting the increase of a number of azobenzene groups within a brush. The overlapping area between the histograms for $\rho_{az}(z)$ and $\rho_{ph}(z)$ is proportional to the probability to find both types of beads in the same z-segment. As it is evident from the figure, with the raise of ρ_g from 0.019 to 0.076, the overlap area grows, with the main effect being the increase of the number of azobenzenes in a brush. With the further raise of ρ_g up to 0.135, this area decays. The main effect here is the brush entering the regime of a dense brush, with the consequence that the LDLs are expulsed from the brush because of the excluded volume effects.

Quantitatively, the probability of an azobenzene to meet a phospholipid at the same specified distance z from the bottom wall is given by the joint probability, $\rho_{az}(z)\rho_{az}(z)$. It is displayed in Figure 6a for the case of $l_{bb} = 16$ and a range of grafting densities ρ_g. The global probability for an azobenzene and phospholipid to be found at the same z is given by

$$p = \int_0^{L_z} \rho_{az}(z)\rho_{ph}(z)\, dz. \tag{7}$$

Figure 6b shows its dependence on the grafting density of a brush, ρ_g, at various lengths of a polymer backbone, l_{bb}. It is evident that at each backbone length $l_{bb} \geq 10$, there is a specific value for the grafting density, ρ_g^*, at which p reaches its maximum value, as

indicated in Figure 6b. One, however, should take into account that the number of available azobenzenes per square area of a brush is proportional not only to the chains grafting density, ρ_g, but also to their number in a single chain, $n_{sc} = \mathrm{div}(l_{bb}, 2)$. Therefore, it makes sense to express the probability p also in terms of the azobenzene surface density ρ_{az}

$$\rho_{az} = N_{az} D^2 / (L_x L_y) = \rho_g n_{sc} (D/\sigma)^2, \tag{8}$$

where N_{az} is the total number of azobenzenes on a single wall functionalised by a brush. The dependence $p(\rho_{az})$, shown in Figure 6c, is practically the same and almost linear in ρ_{az} in the interval $\rho_{az} < 0.3$ for all backbone lengths. Therefore, in this interval of grafting densities, the probability p of an azobenzene and phospholipid to meet at the same z is governed principally by the number of available azobenzenes. At $\rho_{az} > 0.3$, the curves saturate, indicating that the additional number of azobenzenes does not increase the probability p. This is attributed to a gradual expulsion of azobenzenes from the dense brush interior, see Figure 5c, and inaccessibility of azobenzenes adjacent to the wall for interacting with the LDL phospholipids. Therefore, for each given backbone length, l_{bb}, there exists some optimal brush grafting density ρ_g^*, as specified in Figure 6b, and the further increase of ρ_g beyond this value does not increase the probability for the azobenzene and phospholipid to meet at the same z.

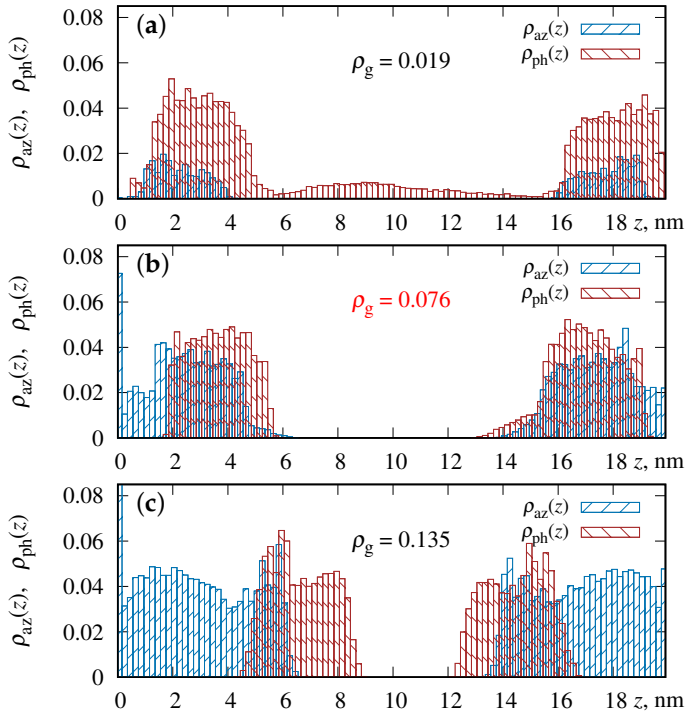

Figure 5. Density profiles for azobenzenes of a brush, $\rho_{az}(z)$, and for phospholipids of LDLs, $\rho_{ph}(z)$, shown for the case of the backbone length $l_{bb} = 16$ and three grafting densities: $\rho_g = 0.019$ (**a**), 0.076 (**b**), and 0.135 (**c**). Note the gradual expulsion of LDL phospholipids away from the brush-rich regions towards the center of a pore with the increase of ρ_g.

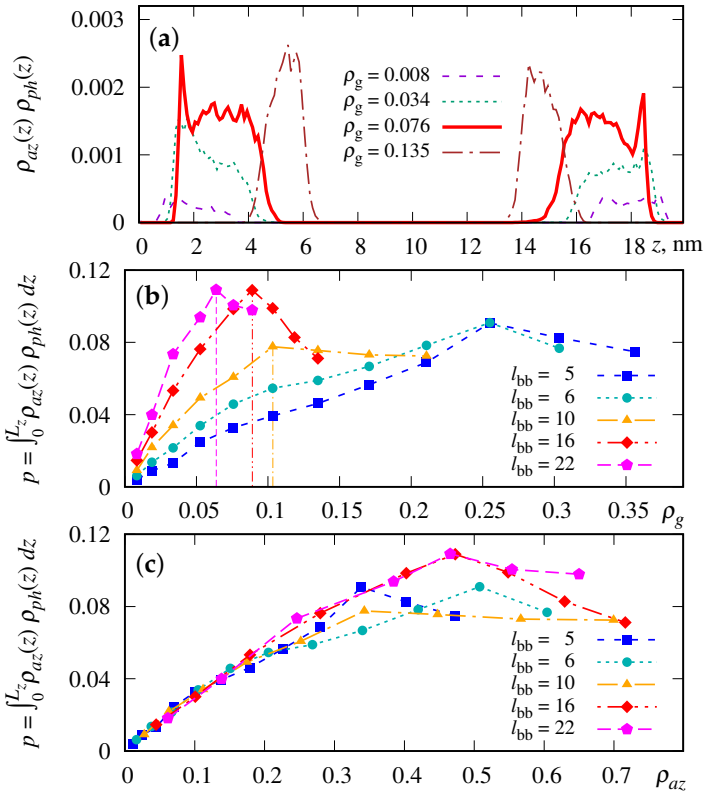

Figure 6. (**a**) Joint probability $\rho_{az}(z)\rho_{ph}(z)$ profile for the backbone length $l_{bb} = 16$ displayed at the set of grafting densities ρ_g indicated in the plot. (**b**) The integral p of a joint probability defined in Equation (7) as a function of grafting density ρ_g at various backbone lengths l_{bb}. Indicated maxima positions are: $\rho_g^* = 0.103$, 0.089, and 0.064 for the backbone lengths $l_{bb} = 10$, 16, and 22, respectively. (**c**) The same as in (**b**) expressed as the function of a surface number density of azobenzenes, ρ_{az}, in a brush.

3.2. Binding Energy of LDLs

A more direct and standard measure of the adsorption efficiency is the binding energy, E_{bind}, evaluated per single LDL particle. In our simulations we define it as the magnitude of the sum of all negative pairwise interaction energies, V_{ij}, between the azobenzene–phospholipid pairs $\langle i, j \rangle$, divided by the number of the LDL particles

$$E_{\text{bind}} = \frac{1}{N_{LDL}} \left| \sum_{\langle i,j \rangle} V_{ij} \right|, \qquad \text{if} \quad V_{ij} = V_{\text{NB}}^{\text{SAP}}[d'(\mathbf{q}_{ij})] < 0. \tag{9}$$

The expression for the azobenzene–phospholipid interaction energy is provided in Equation (1). E_{bind} is displayed, in $k_B T$ units, in Figure 7. For example, Figure 7a shows it as the function of the grafting density ρ_g, whereas Figure 7b as the function of azobenzene surface density ρ_{az}. We note that the exact value for the binding energy depends on both the parameters of the interaction potential between azobenzenes and phospholipids (1) and on the number of interacting pairs. These parameters have not been tuned to match chemical details of the setup and experimental conditions. Therefore, in our study, we concentrate on the relative changes in binding energy upon the variation of the polymer length and the brush density.

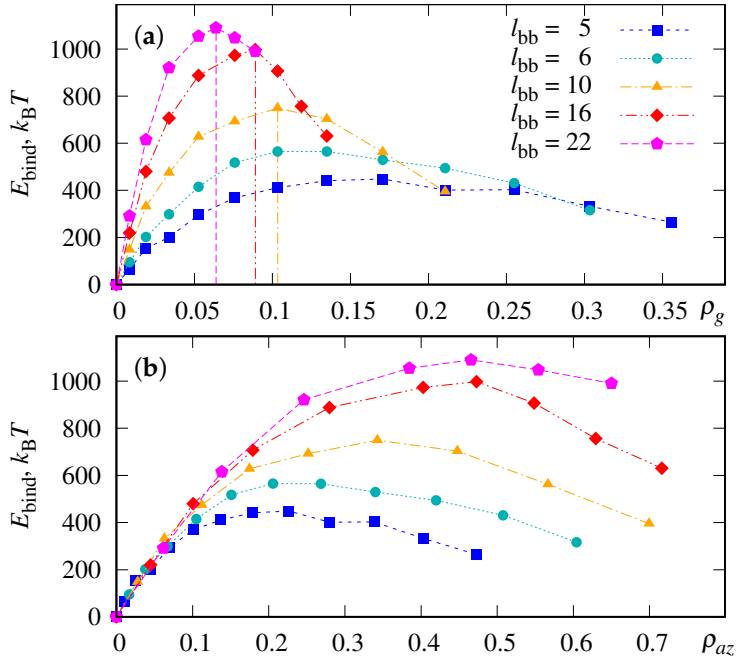

Figure 7. (**a**) Binding energy per single LDL particle, E_{bind}, in units of k_BT, as the function of the grafting density ρ_g. Indicated maxima positions, $\rho_g^* = 0.103$, 0.089, and 0.064, for the backbone length $l_{bb} = 10$, 16, and 22, respectively, are the same as in Figure 6b. (**b**) The same expressed as the function of the azobenzene surface density ρ_{az} given by Equation (8). Backbone lengths l_{bb} are indicated in the figure.

The first thing to note here is that the dependence of E_{bind} has a similar shape to the probability p in Figure 6b, with the maximum reached at the very same characteristic respective values ρ_g^*. This indicates that the magnitude of binding energy is essentially driven by a probability for azobenzenes and phospholipids to meet at the same z, given by p. On the other hand, comparing Figures 6c and 7b, one sees that E_{bind} reaches progressively higher values with the increase of l_{bb} at the same ρ_{az} for $\rho_{az} > 0.1$. Hence, there is another additional factor that increases the number of azobenzene–phospholipid pairs upon the increase of the chain length, which occurs at an almost constant value of the probability p.

3.3. Polymer Bending Effect

This additional factor is the presence of specific conformations of polymer chains. It is quite obvious that because of a finite curvature of the LDL particles, achieving the maximum number of azobenzene–phospholipid contacts and, thus, the largest magnitude for the binding energy, requires essential bending of the polymer chains. Such "wrap over" conformations of polymer chains are illustrated in the snapshot extracted from our simulations and shown in Figure 8.

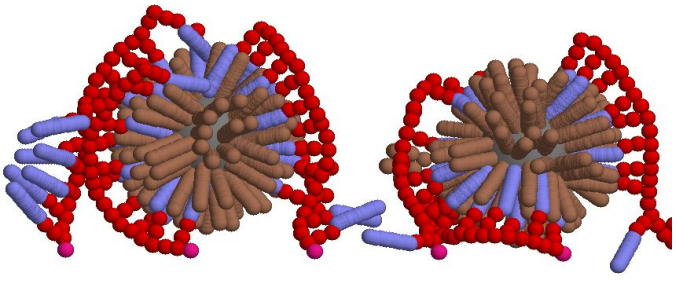

Figure 8. A fragment of a snapshot with the focus on polymer bending in a form of "wrap over" the LDL particle during adsorption of the latter. The case of $l_{bb} = 22$ is shown.

The most probable radius of curvature R^* for the backbone, in the case of an ideal wrap over scenario, can be estimated from the dimensions of all involved beads provided in Section 2. This results in $R^* \approx 3.3$ nm; the value is, of course, dependent on the diameter of the LDL particles. Such bend conformation demands, on one hand, sufficient flexibility of a polymer chain and, on another hand, conditions that there is enough free volume around a chain to bend. The effective value of R^* is expected to increase both at high brush grafting densities (because of straightening up of polymer chains) and at high concentration of adsorbed LDLs (in which case one chain may be in contact with two adjacent LDLs).

To examine the presence of bend conformations, we analyse each polymer of a brush separately. The beads comprising the chosen backbone are fitted to the spherical surface using the algorithm that reduces this problem to the linear least squares problem [65]. The latter has been solved in Refs. [66–68] and is available in a form of an open source FORTRAN-90 package via GitHub [69]. The radius R of a spherical surface that fits the spatial distribution of backbone beads the best and provides the estimate for its radius of curvature.

We built the distributions, $f(R)$, of such radii of curvature, R, and these are shown in Figure 9 for four backbone lengths, $l_{bb} = 6$, 10, 16, and 22, and a set of characteristic grafting densities, ρ_g, including optimal density ρ_g^*, in each case. Let us consider the case of a short backbone, $l_{bb} = 6$, first, shown in Figure 9a. It is evident that the distributions $f(R)$ are very much the same within the broad interval of grafting densities, $0.008 < \rho_g < 0.303$, with the maximum of the distribution positioned at $R \approx R^*$. It is so because the chain length is much smaller than the diameter of LDL, and such chains easily follow the curvature of the LDL surface. For the case of a longer backbone, $l_{bb} = 10$, the increase of the grafting density leads to broadening of the $f(R)$ distribution and shifting the maximum position to higher values (see Figure 9b). This reflects straightening of some polymers when the brush enters the dense brush regime. The same tendency is found upon a further increase of backbone length to $l_{bb} = 16$ and $l_{bb} = 22$ (see Figure 9c,d). Optimal densities, ρ_g^*, as found in Figures 6b and 7a, are highlighted as thicker black curves. At these respective densities, a peak at $R \approx R^*$ is still retained, indicating the presence of the wrap over conformations of chains around the LDL particles. Further increase of the density, $\rho_g \geq 0.103$ for $l_{bb} = 16$ and $\rho_g \geq 0.076$ for $l_{bb} = 22$, eliminates this peak completely reflecting both straightening of polymer chains in the dense brush regime.

3.4. Concluding Remarks on Adsorption Efficiency

The plots for the probability p, Figure 6b, and for the binding energy, Figure 7a, are revisited according to the distributions for the radius of curvature, Figure 9b–d at the same parameters of the chains. In particular, at $\rho_g < \rho_g^*$, the distributions $f(R)$ have well-defined peaks at $R = R^*$, indicating perfect wrap over conformations, as shown in Figure 8. However, the density of azobenzenes in this case is low, leading to smaller values for E_{bind} (low adsorption efficiency). On the other hand, at $\rho_g > \rho_g^*$, the density of azobenzenes is high, but the peak at $R = R^*$ in the distributions $f(R)$ disappears, indicating a relatively small amount of wrap over conformations of chains, which, in turn, leads to the reduction of the value of E_{bind} (low adsorption efficiency). Specific densities ρ_g^* are attributed to a good compromise between these two factors when the density of azobenzenes is sufficiently high and, at the same time, there is abundance of wrap over conformations of polymer chains that ensure sufficient number of the azobenzne–phospholipid close contacts. As a result of this compromise, the binding energy reaches its maximum value (high adsorption efficiency).

Therefore, one can suggest the explanation why the maximum value for binding energy increases at the increase of chain length, l_{bb} (see Figure 7). The shorter chains are able to wrap over the sides of LDLs only, whereas longer chains are able to wrap over the external poles of LDLs as well, thus increasing the number of interacting pairs. This is shown in a series of snapshots in Figure 10.

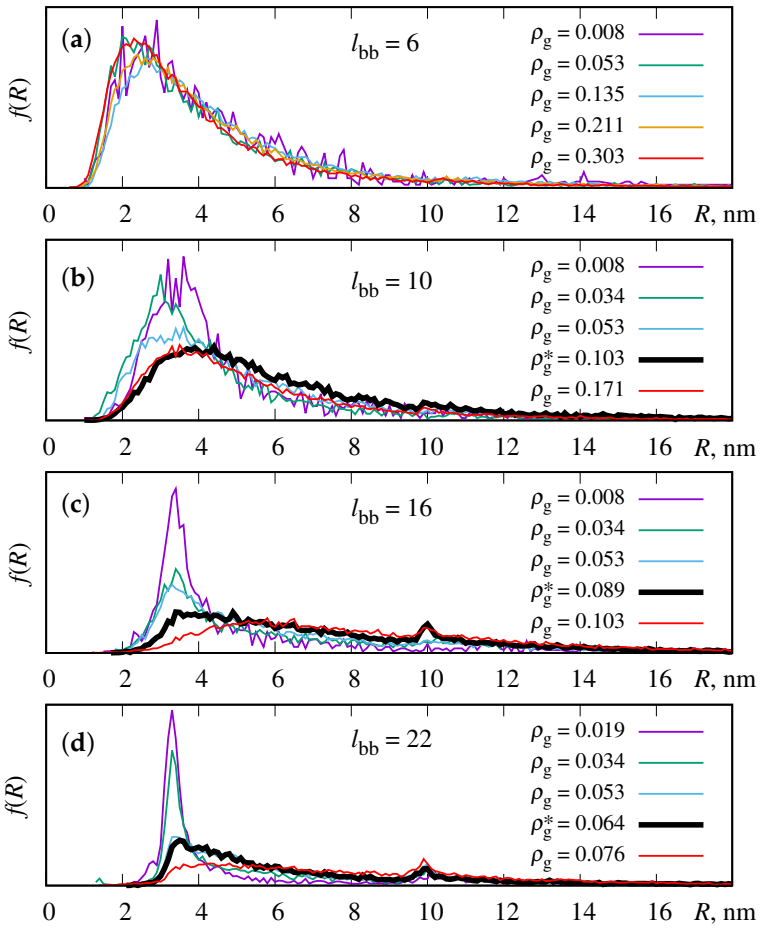

Figure 9. Distributions $f(R)$ for the radius of curvature, R, evaluated for each backbone by mapping its beads onto a spherical surface. (**a**–**d**) show the results for the backbone lengths l_{bb} = 6, 10, 16, and 22, respectively. Specific grafting densities, defined as the maxima positions in Figure 6b, are shown via thick black curves.

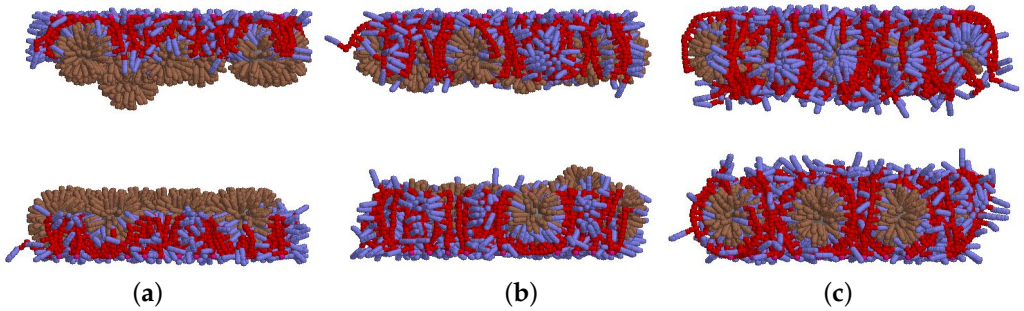

Figure 10. Snapshots visualising the role of a backbone length, l_{bb} = 10, 16, and 22, in adsorption of LDLs. In each case, the respective optimal grafting density obtained in Figures 6c and 7b is used. (**a**) l_{bb} = 10, ρ_g = 0.10; (**b**) l_{bb} = 16, ρ_g = 0.09; (**c**) l_{bb} = 22, ρ_g = 0.064.

At $\rho > \rho_g^*$, the excluded volume effects are brought into play and the brush expulses LDLs, and thus, E_{bind} decays because of a reduced number of interacting azobenzene–phospholipid pairs. This arrangement of the brush and of the LDL particles is shown in Figure 11.

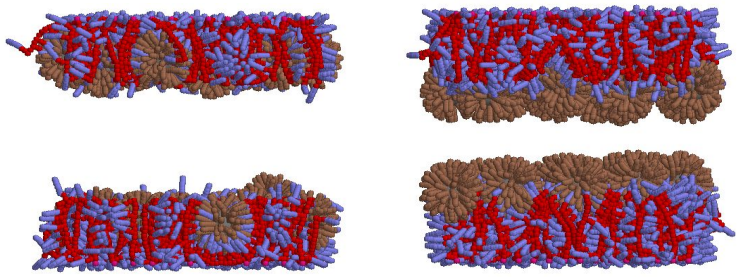

(**a**) (**b**)

Figure 11. Snapshots visualising the role of grafting density in adsorption of LDLs at a fixed backbone length $l_{bb} = 16$. (**a**) Optimal grafting density of $\rho_g = 0.089$ and (**b**) higher grafting density of $\rho_g = 0.135$. (**a**) $l_{bb} = 16$, $\rho_g = 0.089$; (**b**) $l_{bb} = 16$, $\rho_g = 0.135$.

The results of this section lead to the following conclusions. Firstly, at each fixed length of polymer chains, given by its backbone length l_{bb}, the grafting density ρ_g^* exists that is optimal for the LDL adsorption. The efficiency of the latter is characterised by the binding energy E_{bind} per one LDL, as shown in Figure 7. The increase of adsorption efficiency at low ρ_g should be attributed to the increase of azobenzene density in the region accessible to LDLs, whereas the decrease of adsorption efficiency at higher ρ_g is related both to the straightening of chains reducing the azobenzene–phospholipid contacts and to the excluded volume effects in a regime of a dense brush (see Figure 11b). Secondly, with the increase of the backbone length, l_{bb}, the adsorption efficiency increases until it starts to saturate, as seen in Figure 7. The initial increase is related to the growth of a number of available azobenzenes for binding, see Figure 10, whereas the saturation occurs when the brush height reaches the diameter of the LDL particle, see the Figure 10c. Thirdly, an efficient adsorption requires the ability of polymer chains to bend and to wrap over the LDL particles, as shown in Figures 8 and 9. However, in reality, this factor will depend strongly on the polymer chain flexibility and the relation between the chain length and the diameter of an LDL particle.

4. Adsorber Regeneration under Ultraviolet Light

Azobenzene-containing smart LDL adsorber, as suggested and tested in Ref. [21], allows for clean and efficient regeneration and reusage. This can be achieved by illumination of an adsorber by UV light with a suitable wavelength. In this case, the azobenzenes in a polymer brush undergo the *trans*-to-*cis* photo-isomerisation [70] and lose their liquid crystalline and apolar features. As a result, their interaction with phospholipids weakens, and the LDL particles desorb from the polymer brush of an adsorber. The LDL particles can be washed out of the adsorber and the latter can be reused, with a reported recovery rate of 97.9% after five regeneration cycles [21].

In terms of the modelling approach, described in detail in Section 2, the *trans*-to-*cis* photo-isomerisation is mimicked via switching the interaction potential between the azobenzene and phospholipid spherocylinders from the attractive (1) to a repulsive (3) form.

Figure 12 shows a series of snapshots demonstrating gradual desorption of LDLs from a polymer brush of the backbone length $l_{bb} = 10$ and with, optimal for adsorption, a grafting density of $\rho_g^* = 0.103$. Figure 12a shows the initial, adsorbed state, obtained after 40 ns under normal conditions (see Section 3). In this state, the azobenzenes are in the *trans*-state indicated by their blue colouring. Upon switching on the UV light, azobenzenes photoisomerise into their *cis*-form indicated by yellow colouring, and the process of desorption starts. At its first stage, Figure 12b, both bottom and top layers of LDLs are pushed out of the brush but retain their layered structure. After some illumination time, indicated in the figure, the layers are destroyed and LDLs fill the bulk central region of a pore uniformly (see Figure 12c). Now they can be easily washed out of the pore by a flow.

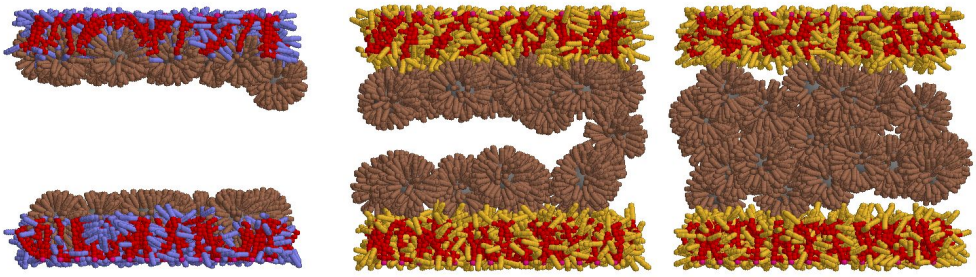

Figure 12. Snapshots showing the desorption dynamics of LDLs on a double-wall brush composed of side-chain polymers of the backbone length $l_{bb} = 10$ (5 side chains in each chain terminated by the azobenzene bead) at grafting density $\rho_g^* = 0.103$ under UV light. (**a**) visualises the initial system with adsorbed LDLs; (**b**,**c**) the system after illumination for 0.6 ns and 4 ns, respectively. Yellow scpherocylinders represent beads with the properties of *cis*-isomers of azobenzene. (**a**) Initial; (**b**) after 0.6 ns under UV; (**c**) after 4 ns under UV.

The issue of interest is the dynamics of desorption of LDLs under UV light compared to their adsorption under normal conditions, covered in Section 3. For this purpose, we cannot use the binding energy E_{bind} (7), as it instantly drops to zero when all azobenzenes switch into a *cis* state. However, as it was shown in Section 3, its behaviour is very similar to that for p, the probability to find the azobenzene and phospholipid at the same distance from the bottom wall (see Figure 6). We used this probability as a rough estimate for the LDL adsorption and desorption dynamics. The results are shown in Figure 13 for three backbone lengths, $l_{bb} = 10$, 16, and 22 at their respective optimal brush densities, as obtained in Figure 7.

The first observation that stems from Figure 13 is that there is a saturation in the temporal behaviour of p at $l_{bb} \geq 16$ (see Figure 13a). The second thing to mention is that the desorption dynamics at $l_{bb} = 22$ is essentially slower than for two other cases, $l_{bb} = 10$ and 16 (see Figure 13b). We explain this by essential reduction of the volume of a bulk region of a pore in the case of the longest chain and, as a result, slowing down its diffusion required for the desorption. Finally, perhaps, the main result is that the rate of desorption, shown in Figure 13a, is essentially higher than that for adsorption, shown in Figure 13b.

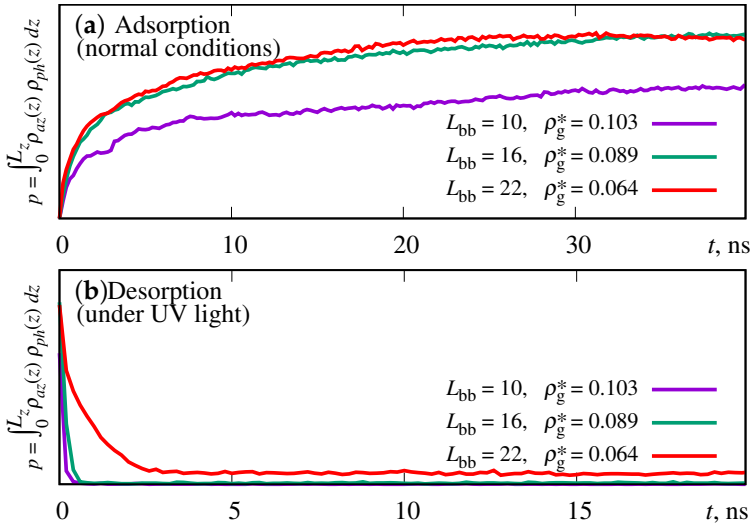

Figure 13. (**a**) Time evolution of the global probability for an azobenzene and phospholipid to be found at the same distance z from the bottom wall, p (see Equation (7)), during the process of adsorption under normal conditions. Three cases of the backbone length l_{bb} are shown at their respective optimal densities, ρ_g^*, (see Section 3). (**b**) The same during the process of desorption under UV light.

5. Conclusions

The study was motivated by the experimental results by Guo et al. [21], where the authors presented an advanced adsorber in a form of a photo-sensible smart surface, and examined its efficiency towards selective adsorption of LDL particles in the course of a hemoperfusion protocol. Besides the definite success of these experimental findings, the question arises how the very details of the molecular architecture of such adsorber affects the efficiency of adsorption. The progress in this direction can be attempted by employing computer simulations.

The nature of LDL adsorption is extremely complex and involves a range of relevant length and time scales. Indeed, microscopically, it is governed by highly specific atomic interactions between the functional groups of a brush and those of the LDL particle, particularly, the phospholipids. On the other hand, adsorption manifests itself in a statistical way, in a system with a considerable number of polymer chains and LDL particles, and is the result of the competition between various interaction effects being involved in this process. In this study, we address the latter, statistical, aspect of the LDL adsorption, which inevitably leaves us with the only option to coarse-grain the principal interactions (i) within a polymer brush, (ii) within each LDL particle, and (iii) between relevant groups of both. This follows the philosophy of some of our previous studies, including azobenzene-containing polymeric systems [40–43].

The diameter of a model LDL particle is about five times smaller than that of its real counterpart. Another simplification is based on the fact that the diameter of spherical adsorbers used in Ref. [21] are ten times larger than the diameter of the LDL particle. Therefore, we replaced the curved surface of such adsorber by a flat surface. The polymer chains of a brush are of the side-chain architecture with their backbones and side chain made of soft-core repulsive spherical beads. A range of backbone lengths, $l_{bb} = 5 - 22$ spherical beads, are considered such that the longest polymer length does not exceed the diameter of the LDL particle. Their side chains are terminated by the azobenzene groups, represented by soft-core repulsive spherocylinders. The LDL particle comprises a spherical core, which represents uniformly packed cholesteryl esters and triglycerides, surrounded by a shell of phospholipid groups modelled by the same spherocylinder beads. To simplify the description, only the azobenzene–phospholipid interaction is made attractive, and it governs the adsorption process. Due to the nature of the soft-core interactions, the dynamics in the system are artificially sped-up and, therefore, does not reflect the dynamics in a real system.

Under normal conditions, LDLs are adsorbed by a smart surface on both walls of a pore—this takes up to 40 ns in model time units. Assuming that the adsorption efficiency will depend on the probability for the azobezene and phospholipid beads to meet in the same segment of a pore, we evaluate the probability, p, of such an event first. Its behaviour with the grafting density of a brush, ρ_g, indicated the presence of some optimal value for ρ_g^*, at which p reaches its maximum value. At $\rho > \rho_g^*$, the value of p decreases, as the LDL particles are pushed out of a dense brush because of the excluded volume interactions. One, however, observes that if p is replotted in terms of the azobenzene density, it shows weak or no dependence on a backbone length l_{bb}.

A more direct measure of the adsorption efficiency is provided by the magnitude of binding energy, E_{bind}, which shows the similar dependence on ρ_g to that for the probability p, but indicates higher adsorption efficiency with the increase of l_{bb} until it saturates at $l_{bb} > 22$, when the chain length reaches the values comparable to the diameter of the LDL particle. The explanation of this dependence is found by analysing the curvature of chains in all cases being considered. In particular, at $\rho_g \leq \rho_g^*$, the longer chains are found to be able to bend over both the sides and the top of LDL particles, thus increasing E_{bind}. At $\rho_g \leq \rho_g^*$, the radius of curvature is found to increase, essentially indicating straightening of the chains, the effect characteristic of the dense brush regime. This factor, which prevents chains from bending over the LDL particles and, thus, reducing the number of azobenzene–

phospholipid contacts, also contributes to the decrease of E_{bind}, alongside the excluded volume effect within the brush interior.

The results obtained here indicate that **optimal adsorption efficiency** is achieved as a result of compromise between several factors. The **grafting density** should be high enough to provide sufficiently high concentration of azobenzenes but below the dense brush threshold to avoid expulsion of LDL from a brush due to strong excluded volume effects. Polymer chains of a brush should be **flexible** enough to allow polymer wrap over LDLs and their characteristic **length** be of an order of half of the LDL circumference.

Under UV light, the model brush is found to clear up quickly, requiring up to 1 ns time in model time units. It occurs in two stages. At the first stage, LDLs desorb from both smart surfaces while preserving their layered structure, whereas at the second stage, they lose this structure and are distributed uniformly within a pore interior clear of brush regions. We found that the dynamics of desorption are at least one order of magnitude faster than that for adsorption.

The study opens up future refinements and extensions. In particular, one can match parameters of a model more closely to that for real systems through the incorporation of some variant of a multiscale approach. One can also consider the mixture of the LDL and HDL particles and model a selective interaction between the brush and both types of lipoproteins. Various branched molecular architectures can be tested for adsorption efficiency. Finally, one can study adsorption/desorption cycles under flow introduced within a pore to mimic realistic situations found in the experimental setup. These cases are reserved for future studies.

Author Contributions: Medical aspects and conceptualization, J.I. and O.K.; simulation methodology, software, performing simulation runs, J.I. and D.Y.; validation and formal analysis, J.I., D.Y.; interpretation, J.I., D.Y. and O.K.; writing—original draft preparation, J.I.; writing—review and editing, J.I., O.K. and D.Y.; visualization, J.I. All authors have read and agreed to the published version of the manuscript.

Funding: DY acknowledges partial support from the NAS of Ukraine (the grant for research laboratories/groups of young scientists No 07/01-2022(4)).

Data Availability Statement: The data presented in this study are available on request from the corresponding author.

Acknowledgments: The authors are grateful to the Armed Forces of Ukraine for protection during the time this research was undertaken.

Conflicts of Interest: The authors declare no conflict of interest.

References

1. Sacks, F.M.; Campos, H. Low-Density Lipoprotein Size and Cardiovascular Disease: A Reappraisal. *J. Clin. Endocrinol. Metab.* **2003**, *88*, 4525–4532. [CrossRef] [PubMed]
2. Sikorski, J. Atherosclerosis/lipoprotein/cholesterol metabolism. In *Comprehensive Medicinal Chemistry II*; Elsevier: Amsterdam, The Netherlands, 2007; pp. 459–494. [CrossRef]
3. Mundi, S.; Massaro, M.; Scoditti, E.; Carluccio, M.A.; van Hinsbergh, V.W.M.; Iruela-Arispe, M.L.; Caterina, R.D. Endothelial permeability, LDL deposition, and cardiovascular risk factors—A review. *Cardiovasc. Res.* **2017**, *114*, 35–52. [CrossRef] [PubMed]
4. Kiberstis, P.A. Fatty liver—Too much of a bad thing? *Science* **2019**, *364*, 1044.6–1045. [CrossRef]
5. Thierer, J.H.; Ekker, S.C.; Farber, S.A. The LipoGlo reporter system for sensitive and specific monitoring of atherogenic lipoproteins. *Nat. Commun.* **2019**, *10*, 3426. [CrossRef] [PubMed]
6. Yu, Y.; Dong, J.; Ma, B.; Jiang, X.; Guo, C.; Liu, Z.; Chai, Y.; Wang, L.; Sun, L.; Ou, L.; et al. Bio-inspired dual-functional phospholipid–poly(acrylic acid) brushes grafted porous poly(vinyl alcohol) beads for selective adsorption of low-density lipoprotein. *J. Mater. Chem. B* **2021**, *9*, 6364–6376. [CrossRef]
7. Cheng, Y.; Wang, S.; Yu, Y.; Yuan, Y. In vitro, in vivo studies of a new amphiphilic adsorbent for the removal of low-density lipoprotein. *Biomaterials* **2003**, *24*, 2189–2194. [CrossRef]
8. Yu, Y.; Ma, B.; Jiang, X.; Guo, C.; Liu, Z.; Li, N.; Chai, Y.; Wang, L.; Du, Y.; Wang, B.; et al. Amphiphilic shell nanomagnetic adsorbents for selective and highly efficient capture of low-density lipoprotein from hyperlipidaemia serum. *J. Mater. Chem. B* **2022**, *10*, 4856–4866. [CrossRef]

9. Lanzalaco, S.; Armelin, E. Poly(N-isopropylacrylamide) and Copolymers: A Review on Recent Progresses in Biomedical Applications. *Gels* **2017**, *3*, 36. [CrossRef]
10. Sudre, G.; Siband, E.; Gallas, B.; Cousin, F.; Hourdet, D.; Tran, Y. Responsive Adsorption of N-Isopropylacrylamide Based Copolymers on Polymer Brushes. *Polymers* **2020**, *12*, 153. [CrossRef]
11. Yaremchuk, D.; Kalyuzhnyi, O.; Ilnytskyi, J. Modelling thermoresponsive polymer brush by mesoscale computer simulations. *Condens. Matter Phys.* **2023**, *26*, 33302. [CrossRef]
12. Tian, L.; Dou, H.; Shao, Y.; Yi, Y.; Fu, X.; Zhao, J.; Fan, Y.; Ming, W.; Ren, L. Magnetically controlled super-wetting surface switching between ultra-low and ultra-high droplet adhesion. *Chem. Eng. J.* **2023**, *456*, 141093. [CrossRef]
13. Malm, J.; Sahramo, E.; Karppinen, M.; Ras, R.H.A. Photo-Controlled Wettability Switching by Conformal Coating of Nanoscale Topographies with Ultrathin Oxide Films. *Chem. Mater.* **2010**, *22*, 3349–3352. [CrossRef]
14. Bahl, S.; Nagar, H.; Singh, I.; Sehgal, S. Smart materials types, properties and applications: A review. *Mater. Today Proc.* **2020**, *28*, 1302–1306. [CrossRef]
15. Zhao, Y. *Smart Light-Responsive Materials*; Wiley-Blackwell: Hoboken, NJ, USA, 2009.
16. Roling, O.; Stricker, L.; Voskuhl, J.; Lamping, S.; Ravoo, B.J. Supramolecular surface adhesion mediated by azobenzene polymer brushes. *Chem. Commun.* **2016**, *52*, 1964–1966. [CrossRef] [PubMed]
17. Santer, S. Remote control of soft nano-objects by light using azobenzene containing surfactants. *J. Phys. D Appl. Phys.* **2017**, *51*, 013002. [CrossRef]
18. Wu, Z.; Li, X.; Jiang, X.; Xie, T.; Li, H.; Zhang, G.; Jiang, J. Photoswitchable de/adsorption of an azobenzene-derived surfactant on a silica surface. *Phys. Chem. Chem. Phys.* **2019**, *21*, 21030–21037. [CrossRef]
19. Hisham, S.; Sarih, N.M.; Tajuddin, H.A.; Abidin, Z.H.Z.; Abdullah, Z. Unraveling the surface properties of PMMA/azobenzene blends as coating films with photoreversible surface polarity. *RSC Adv.* **2021**, *11*, 15428–15437. [CrossRef]
20. Mukai, K.; Imai, K.; Hara, M.; Nagano, S.; Seki, T. A High-Density Azobenzene Side Chain Polymer Brush for Azimuthal and Zenithal Orientational Photoswitching of a Nematic Liquid Crystal. *ChemPhotoChem* **2019**, *3*, 495–500. [CrossRef]
21. Guo, C.; Yu, Y.; Jiang, X.; Ma, B.; Liu, Z.; Chai, Y.; Wang, L.; Wang, B.; Du, Y.; Li, N.; et al. Photorenewable Azobenzene Polymer Brush-Modified Nanoadsorbent for Selective Adsorption of LDL in Serum. *ACS Appl. Mater. Interfaces* **2022**, *14*, 34388–34399. [CrossRef]
22. Antwerpen, R.V.; Gilkey, J.C. Cryo-electron microscopy reveals human low density lipoprotein substructure. *J. Lipid Res.* **1994**, *35*, 2223–2231. [CrossRef]
23. Orlova, E.V.; Sherman, M.B.; Chiu, W.; Mowri, H.; Smith, L.C.; Gotto, A.M. Three-dimensional structure of low density lipoproteins by electron cryomicroscopy. *Proc. Natl. Acad. Sci. USA* **1999**, *96*, 8420–8425. [CrossRef] [PubMed]
24. Hevonoja, T.; Pentikäinen, M.O.; Hyvönen, M.T.; Kovanen, P.T.; Ala-Korpela, M. Structure of low density lipoprotein (LDL) particles: Basis for understanding molecular changes in modified LDL. *Biochim. Biophys. Acta (BBA) Mol. Cell Biol. Lipids* **2000**, *1488*, 189–210. [CrossRef]
25. Segrest, J.P.; Jones, M.K.; Loof, H.D.; Dashti, N. Structure of apolipoprotein B-100 in low density lipoproteins. *J. Lipid Res.* **2001**, *42*, 1346–1367. [CrossRef] [PubMed]
26. Teerlink, T.; Scheffer, P.G.; Bakker, S.J.; Heine, R.J. Combined data from LDL composition and size measurement are compatible with a discoid particle shape. *J. Lipid Res.* **2004**, *45*, 954–966. [CrossRef]
27. Ren, G.; Rudenko, G.; Ludtke, S.J.; Deisenhofer, J.; Chiu, W.; Pownall, H.J. Model of human low-density lipoprotein and bound receptor based on CryoEM. *Proc. Natl. Acad. Sci. USA* **2009**, *107*, 1059–1064. [CrossRef]
28. Kumar, V.; Butcher, S.J.; Öörni, K.; Engelhardt, P.; Heikkonen, J.; Kaski, K.; Ala-Korpela, M.; Kovanen, P.T. Three-Dimensional cryoEM Reconstruction of Native LDL Particles to 16 Å Resolution at Physiological Body Temperature. *PLoS ONE* **2011**, *6*, e18841. [CrossRef]
29. Prassl, R.; Laggner, P. Lipoprotein structure and dynamics: Low density lipoprotein viewed as a highly dynamic and flexible nanoparticle. In *Lipoproteins—Role in Health and Diseases*; InTech: London, UK, 2012. [CrossRef]
30. Heikelä, M.; Vattulainen, I.; Hyvönen, M.T. Atomistic Simulation Studies of Cholesteryl Oleates: Model for the Core of Lipoprotein Particles. *Biophys. J.* **2006**, *90*, 2247–2257. [CrossRef]
31. Vattulainen, I.; Rog, T. Lipid Simulations: A Perspective on Lipids in Action. *Cold Spring Harb. Perspect. Biol.* **2011**, *3*, a004655. [CrossRef]
32. Murtola, T.; Vuorela, T.A.; Hyvönen, M.T.; Marrink, S.J.; Karttunen, M.; Vattulainen, I. Low density lipoprotein: Structure, dynamics, and interactions of apoB-100 with lipids. *Soft Matter* **2011**, *7*, 8135. [CrossRef]
33. Koivuniemi, A.; Vuorela, T.; Kovanen, P.T.; Vattulainen, I.; Hyvönen, M.T. Lipid Exchange Mechanism of the Cholesteryl Ester Transfer Protein Clarified by Atomistic and Coarse-grained Simulations. *PLoS Comput. Biol.* **2012**, *8*, e1002299. [CrossRef]
34. Lewis, D.R.; Kholodovych, V.; Tomasini, M.D.; Abdelhamid, D.; Petersen, L.K.; Welsh, W.J.; Uhrich, K.E.; Moghe, P.V. In silico design of anti-atherogenic biomaterials. *Biomaterials* **2013**, *34*, 7950–7959. [CrossRef] [PubMed]
35. Antonijevic, T.; Lancaster, J.L.; Starobin, J.M. Modeling order-disorder transition in Low-Density Lipoprotein. In Proceedings of the 2014 36th Annual International Conference of the IEEE Engineering in Medicine and Biology Society, Chicago, IL, USA, 26–30 August 2014. [CrossRef]
36. Cilpa-Karhu, G.; Jauhiainen, M.; Riekkola, M.L. Atomistic MD simulation reveals the mechanism by which CETP penetrates into HDL enabling lipid transfer from HDL to CETP. *J. Lipid Res.* **2015**, *56*, 98–108. [CrossRef]

37. Angarica, V.E.; Orozco, M.; Sancho, J. Exploring the complete mutational space of the LDL receptor LA5 domain using molecular dynamics: Linking SNPs with disease phenotypes in familial hypercholesterolemia. *Hum. Mol. Genet.* **2016**, *25*, 1233–1246. [CrossRef]
38. Lei, D.; Rames, M.; Zhang, X.; Zhang, L.; Zhang, S.; Ren, G. Insights into the Tunnel Mechanism of Cholesteryl Ester Transfer Protein through All-atom Molecular Dynamics Simulations. *J. Biol. Chem.* **2016**, *291*, 14034–14044. [CrossRef] [PubMed]
39. Lauer, M.E.; Graff-Meyer, A.; Rufer, A.C.; Maugeais, C.; von der Mark, E.; Matile, H.; D'Arcy, B.; Magg, C.; Ringler, P.; Müller, S.A.; et al. Cholesteryl ester transfer between lipoproteins does not require a ternary tunnel complex with CETP. *J. Struct. Biol.* **2016**, *194*, 191–198. [CrossRef] [PubMed]
40. Ilnytskyi, J.; Slyusarchuk, A.; Saphiannikova, M. Photo-controllable percolation of decorated nanoparticles in a nanopore: Molecular dynamics simulation study. *Math. Model. Comput.* **2016**, *3*, 33–42. [CrossRef]
41. Ilnytskyi, J.M.; Slyusarchuk, A.; Saphiannikova, M. Photocontrollable Self-Assembly of Azobenzene-Decorated Nanoparticles in Bulk: Computer Simulation Study. *Macromolecules* **2016**, *49*, 9272–9282. [CrossRef]
42. Ilnytskyi, J.M.; Toshchevikov, V.; Saphiannikova, M. Modeling of the photo-induced stress in azobenzene polymers by combining theory and computer simulations. *Soft Matter* **2019**, *15*, 9894–9908. [CrossRef]
43. Slyusarchuk, A.Y.; Yaremchuk, D.L.; Ilnytskyi, J.M. Adsorption of decorated nanoparticles on a liquid crystalline polymer brush: molecular dynamics study. *Math. Model. Comput.* **2020**, *7*, 207–218. [CrossRef]
44. Yaremchuk, D.; Patsahan, T.; Ilnytskyi, J. Photo-switchable liquid crystalline brush as an aligning surface for liquid crystals: modelling via mesoscopic computer simulations. *Condens. Matter Phys.* **2022**, *25*, 33601. [CrossRef]
45. Austin, M.; Krauss, R. Genetic Control of Low-Density-Lipoprotein Subclasses. *Lancet* **1986**, *328*, 592–595. [CrossRef]
46. Campos, H.; Genest, J.J.; Blijlevens, E.; McNamara, J.R.; Jenner, J.L.; Ordovas, J.M.; Wilson, P.W.; Schaefer, E.J. Low density lipoprotein particle size and coronary artery disease. *Arterioscler. Thromb. A J. Vasc. Biol.* **1992**, *12*, 187–195. [CrossRef] [PubMed]
47. Austin, M.A. Low-Density Lipoprotein Subclass Patterns and Risk of Myocardial Infarction. *JAMA J. Am. Med Assoc.* **1988**, *260*, 1917. [CrossRef]
48. Stampfer, M.J. A Prospective Study of Triglyceride Level, Low-Density Lipoprotein Particle Diameter, and Risk of Myocardial Infarction. *JAMA J. Am. Med Assoc.* **1996**, *276*, 882. [CrossRef]
49. Lamarche, B.; Tchernof, A.; Moorjani, S.; Cantin, B.; Dagenais, G.R.; Lupien, P.J.; Despre´s, J.P. Small, Dense Low-Density Lipoprotein Particles as a Predictor of the Risk of Ischemic Heart Disease in Men. *Circulation* **1997**, *95*, 69–75. [CrossRef]
50. Scheffer, P.G.; Bakker, S.J.L.; Heine, R.J.; Teerlink, T. Measurement of low-density lipoprotein particle size by high-performance gel-filtration chromatography. *Clin. Chem.* **1997**, *43*, 1904–1912. [CrossRef]
51. Ilnytskyi, J.M.; Lintuvuori, J.S.; Wilson, M.R. Simulation of bulk phases formed by polyphilic liquid crystal dendrimers. *Condens. Matter Phys.* **2010**, *13*, 33001. [CrossRef]
52. Ilnytskyi, J.M.; Slyusarchuk, A.; Sokołowski, S. Gelation of patchy ligand shell nanoparticles decorated by liquid-crystalline ligands: Computer simulation study. *Soft Matter* **2018**, *14*, 3799–3810. [CrossRef]
53. Chvez-Snchez, L.; Chvez-Rueda, K.; Victoria, M.; Montoya-Daz, E.; Blanco-Favel, F. The Innate Immune Response Mediated by TLRs in Atherosclerosis. In *Inflammation, Chronic Diseases and Cancer—Cell and Molecular Biology, Immunology and Clinical Bases*; InTech: London, UK, 2012. [CrossRef]
54. Hughes, Z.E.; Wilson, M.R.; Stimson, L.M. Coarse-grained simulation studies of a liquid crystal dendrimer: Towards computational predictions of nanoscale structure through microphase separation. *Soft Matter* **2005**, *1*, 436. [CrossRef] [PubMed]
55. Stillwell, W. Introduction to biological membranes. In *An Introduction to Biological Membranes*; Elsevier: Amsterdam, The Netherlands, 2016; pp. 3–15. [CrossRef]
56. Lintuvuori, J.S.; Wilson, M.R. A new anisotropic soft-core model for the simulation of liquid crystal mesophases. *J. Chem. Phys.* **2008**, *128*, 044906. [CrossRef]
57. Groot, R.D.; Warren, P.B. Dissipative particle dynamics: Bridging the gap between atomistic and mesoscopic simulation. *J. Chem. Phys.* **1997**, *107*, 4423–4435. [CrossRef]
58. Akiyama, H.; Tamada, K.; Nagasawa, J.; Abe, K.; Tamaki, T. Photoreactivity in Self-Assembled Monolayers Formed from Asymmetric Disulfides Having para-Substituted Azobenzenes. *J. Phys. Chem. B* **2002**, *107*, 130–135. [CrossRef]
59. Wilson, M.R. Molecular dynamics simulations of flexible liquid crystal molecules using a Gay-Berne/Lennard-Jones model. *J. Chem. Phys.* **1997**, *107*, 8654–8663. [CrossRef]
60. Chen, Q.; Yu, S.; Zhang, D.; Zhang, W.; Zhang, H.; Zou, J.; Mao, Z.; Yuan, Y.; Gao, C.; Liu, R. Impact of Antifouling PEG Layer on the Performance of Functional Peptides in Regulating Cell Behaviors. *J. Am. Chem. Soc.* **2019**, *141*, 16772–16780. [CrossRef]
61. Ilnytskyi, J.; Wilson, M.R. A domain decomposition molecular dynamics program for the simulation of flexible molecules with an arbitrary topology of Lennard–Jones and/or Gay–Berne sites. *Comput. Phys. Commun.* **2001**, *134*, 23–32. [CrossRef]
62. Ilnytskyi, J.M.; Wilson, M.R. A domain decomposition molecular dynamics program for the simulation of flexible molecules of spherically-symmetrical and nonspherical sites. II. Extension to NVT and NPT ensembles. *Comput. Phys. Commun.* **2002**, *148*, 43–58. [CrossRef]
63. Jerca, F.A.; Jerca, V.V.; Hoogenboom, R. Advances and opportunities in the exciting world of azobenzenes. *Nat. Rev. Chem.* **2021**, *6*, 51–69. [CrossRef]
64. Zannoni, C. *Liquid Crystals and Their Computer Simulations*; Cambridge University Press: Cambridge, UK, 2022. [CrossRef]

65. Jekel, C.F. *Digital Image Correlation on Steel Ball*; University of Stellenbosch: Stellenbosch, South Africa, 2016; Chapter Appendix A; pp. 83–87.
66. Paige, C.C.; Saunders, M.A. LSQR: An Algorithm for Sparse Linear Equations and Sparse Least Squares. *ACM Trans. Math. Softw.* **1982**, *8*, 43–71. [CrossRef]
67. Paige, C.C.; Saunders, M.A. Algorithm 583: LSQR: Sparse Linear Equations and Least Squares Problems. *ACM Trans. Math. Softw.* **1982**, *8*, 195–209. [CrossRef]
68. Saunders, M.A. Solution of sparse rectangular systems using LSQR and CRAIG. *BIT Numer. Math.* **1995**, *35*, 588–604. [CrossRef]
69. LSQR. Available online: https://github.com/jacobwilliams/LSQR (accessed on 23 July 2023).
70. Todorov, T.; Nikolova, L.; Tomova, N. Polarization holography 1: A new high-efficiency organic material with reversible photoinduced birefringence. *Appl. Opt.* **1984**, *23*, 4309. [CrossRef] [PubMed]